Chapter 6

Synthesis and Characterisation of conducting Ceramic Composites SnO_2:$LaNiO_3$

Part of this chapter is published as **Katheriya Tarun**, Sukhdev Pandey, and Shail Upadhyay. "New frontiers in ceramic composites: tunable electromagnetic interference shielding by realizing negative permittivity in SnO_2/$LaNiO_3$ nanocomposites." *Journal of Materials Chemistry C* (2025).

6.1 Introduction

The rapid proliferation of electronic and communication technologies has profoundly reshaped our modern society, resulting in significant progress in computing, telecommunications, and defense systems. However, these developments have also introduced a critical challenge: **Electromagnetic Interference (EMI)**. EMI can degrade the performance of sensitive electronic devices and systems, and in some cases, it poses a threat to human health. While low frequency EMI typically does not have direct effects on human health, it can disrupt communication systems and cause data loss. High frequency EMI, particularly in the radiofrequency range (300 kHz–300 GHz), is a concern for many consumer electronics. For instance, cell phones operate between 0.9–2.4 GHz, Wi-Fi routers at 2.4 GHz, laptops from 300 Hz to 10 MHz, magnetic resonance imaging (MRI) systems between 1 MHz to 340 MHz, and radars typically operate between 8–12 GHz. Long exposures to these high-frequency can be absorbed by human skin, causing localized heating that could lead to tissue damage, non-thermal effects, such as cellular disruption and DNA damage, though definitive evidence remains limited[175,176]. The rise of high-frequency EM waves, especially in the context of next-generation technologies e.g. Artificial Intelligence (AI) with 5G and 6G technologies, necessitates the development of advanced materials for electromagnetic shielding.

In recent studies the shielding effectiveness (SE) of some recently developed composites was outlined[2,177–181]. It is commonly believed that materials used for EMI shielding must be electrically conductive, as higher conductivity generally improves shielding effectiveness[182]. Traditional materials like copper, aluminum, and carbon composites provide limited protection against these frequencies[178,179,183]. Commercially available EMI shielding materials are composites, primarily EMI absorber-type materials, which

combine a conductive phase (to provide free charge carriers) with an insulating matrix (to control charge carrier distribution). Metals, due to their high electrical conductivity, have traditionally been the material of choice for such applications. However, metals have limitations that restrict their use. These include high plasma frequencies ($\omega_p \sim 10^{12}$ Hz), narrow operational bandwidths, and susceptibility to environmental degradation[143]. One alternative is carbon-based materials, which are lightweight and have porous structures that support the absorption of electromagnetic waves through joule heating[184,185]. Despite their potential, these materials often face challenges such as low density and poor homogeneity, particularly when used in thin films and coatings. To achieve the commercially required shielding level (~20 dB), high filler content (typically 40–60%) is often necessary, leading to increased weight and thickness, which limits their suitability for applications where thin, homogeneous coatings are crucial[186]. The limitations of conventional materials, together with the growing demand in the electronics market, have encouraged the exploration of advanced materials, with Metamaterials, specifically epsilon-negative (ENG) materials, offering a potential solution to these challenges.

ENG materials are Metamaterials characterized by negative permittivity ($\varepsilon < 0$), where the electric displacement field (D) opposes the applied electric field (E), leading to reversed polarization and the reflection and attenuation of electromagnetic waves[5]. These properties make ENG materials ideal for EMI shielding, as they can reflect, absorb, and dissipate electromagnetic energy across a wide frequency range. Historically, metals were the primary materials exhibiting negative permittivity proposed by Paul Drude[121]. However, recent studies have shown that certain ceramics, such as La_2NiO_4, $LaMnO_3$, and Sr_2MnO_4 etc. can also display negative permittivity particularly at radio frequencies[123,138,187]. In our prior

work, we demonstrated that $LaNiO_3$, a conducting perovskite, exhibits negative permittivity at room temperature and provides effective EMI shielding along with corrosion resistance[36]. Building on this, we present a novel composite system composed of conducting and insulating ceramics, termed ***conducting ceramic composites*** (CCC), designed to overcome the challenges of traditional ceramic-metal composites (CMCs) and polymer-metal composites (PMCs)[5,35]. In this study, lanthanum nickelate ($LaNiO_3$) is used as the conductive phase, combined with tin dioxide (SnO_2), an insulating ceramic, to control conductivity and charge carrier concentration. The composites exhibit negative permittivity at and above room temperature when a certain filler threshold is reached. This approach offer significant advantages over traditional metal- and carbon-based composites. Unlike metals/ carbon, the conductivity of conducting ceramics can be precisely tuned through doping or by adjusting synthesis parameters, providing a level of control not achievable with metallic systems, which can generally only be modified by varying filler concentration. Another advantage is the comparable densities of the two materials—$LaNiO_3$ (6.91 g/cm^3) and SnO_2 (6.98 g/cm^3)—which makes it easier to achieve homogeneity for low-dimensional applications like thin films and coatings. Achieving homogeneity with metals or carbon-based materials is more challenging due to their higher density contrast (~9 g/cm^3 for metals and ~2 g/cm^3 for carbon-based materials like graphene).

To explore the potential of this composite system, we prepared three SnO_2:$LaNiO_3$ (SLN) composites with varying weight ratios (90:10, 80:20, and 70:30). These samples were characterized through X-ray diffraction (XRD) and scanning electron microscopy (SEM) to confirm their structural and morphological properties. Electrical characterization was conducted by measuring impedance (Z) and phase angle (φ) as functions of temperature (from room temperature to 600°C) and frequency (from 100 Hz to 2 MHz). Finally, to assess their

potential for EMI shielding, scattering parameters (S_{11} and S_{21}) were measured in the 8–12 GHz frequency range using a vector network analyzer. This study demonstrates the potential of conducting ceramic composites as a new approach for EMI shielding, offering a promising alternative to traditional materials.

6.2 Sample Preparation and Characterization

In the literature, value of the dielectric constant of pure SnO_2 is reported to be 10^3 - 10^4 [188] . In our previous work, we have synthesized and experimentally verified that $LaNiO_3$ is inherently conductive in nature and exhibits negative permittivity[36]. Considering the electronic nature of these two compounds, we can apply effective medium theory (EMT) to predict the minimum threshold concentration of $LaNiO_3$ in SnO_2 to achieve negative permittivity.

According to the Maxwell-Garnett model, the effective permittivity of a composite depends on the volume fractions of the inclusions and the host material, as well as their individual permittivity[189,190].

The effective permittivity (ε_{eff}) of a composite with spherical $LaNiO_3$ inclusions in a SnO_2 matrix can be expressed as:

$$\varepsilon_{eff} = \varepsilon_{SnO2}\left[1 + \frac{3c(\varepsilon_{LaNiO3} - \varepsilon_{SnO2})}{\varepsilon_{LaNiO3} + 2\varepsilon_{SnO2} - c(\varepsilon_{LaNiO3} - \varepsilon_{SnO2})}\right] \quad (6.1)$$

Where c is the volume fraction of the $LaNiO_3$.

In an ideal situation, theoretical approximations suggest that the minimum concentration required to achieve negative permittivity is 30%. (ε_{SnO2} ~ 10^3', ε_{LaNiO3} ~ -2 x 10^6). To verify

this, we have carefully selected 10%, 20%, and 30% (by weight) concentration of $LaNiO_3$, to study the transition from isolated $LaNiO_3$ particles (non-percolating system) to interconnected conductive networks (percolating system).

Nano-sized $LaNiO_3$ was synthesized using the sol-gel method. For this study AR grade SnO_2 (Alfa Aesar, purity > 99 %) was purchased commercially. The individual materials (SnO_2 and $LaNiO_3$) were weighed according to their respective wt % and then SLN composite powders were mixed in a planetary ball mill (Retsch PM 200, Germany) with an agate jar (250 mL) and 10.03 mm diameter balls at 120 rpm for 24 h, using acetone as the milling medium. A ball-to-powder weight ratio of 5:1 was maintained. To minimize overheating, agglomeration, and adhesion of the powder to the milling vessel and balls, milling was performed in cycles of 15 min of rotation, followed by 5 min of rest, with alternating clockwise and counterclockwise rotation. The mixture was subsequently dried at 200 °C for 12 h in a conventional oven. These composites were named $90SnO_2$–$10LaNiO_3$ (SLN10), $80SnO_2$–$20LaNiO_3$ (SLN20), and $70SnO_2$–$30LaNiO_3$ (SLN30), where the numerical suffix represents the $wt.\%$ of $LaNiO_3$ in the composite. The dried powder was mixed with 2% polyvinyl alcohol (PVA) as a binder, and then pressed into cylindrical pellets (10.00 x 2.00 mm). The pellets were heat-treated at 700 °C to remove the PVA and increase their compactness and hardness. The pellets were cleaned and polished with different grades of ambry paper to achieve a smooth surface free from any surface contaminants. The X-ray diffraction (XRD) patterns were recorded using a diffractometer (Rigaku X'PERT PRO MPD) with Cu-Kα radiation (λ = 1.5418 Å) over a range of 20° to 80° with a step size of 5°/min. The microstructure of the composites was examined using a scanning electron microscope (SEM, ZEISS, USA). The pellets were coated with conductive silver paste to maintain electrical contact. Impedance was measured using a LCR meter (Keysight E-

4980A) in a frequency range of 100 Hz to 2 MHz and temperatures from 30 °C to 600 °C, at a cooling rate of 3 °C/min.

For shielding effectiveness measurements, the pellets were crushed into fine powder using agate mortar for 30 min. then mixed with clear epoxy resin (80% sample / 20% epoxy), and allowed to cure at room temperature. The dried samples were cut into rectangular shapes with dimensions of 22.03 x 10.05 x 2.00 mm to fit into the X-band waveguide WR90. The Scattering parameters (S-parameters) were recorded using an Agilent PNA-L N5230C Vector Network Analyzer (VNA) in the X-band frequency range of 8.0 to 13.0 GHz. The detailed synthesis process and characterization is shown in Figure 6.1.

Figure 6.1 Schematic illustrating the detailed sample preparation process. (a) Synthesis of pure $LaNiO_3$, (b) Steps involved in composite preparation.

6.3 Results and Discussion

6.3.1 X-ray Diffraction (XRD) Studies

X-ray diffraction (XRD) was performed to examine the phase purity, crystallinity, and to rule out possibilities of chemical reaction between two phases SnO_2 and $LaNiO_3$. Figure 6.2 (a) displays the XRD pattern of SnO_2 and $LaNiO_3$, compared with their respective reference patterns (SnO_2: CIF 1000062; $LaNiO_3$: CIF 1000307). The SnO_2 diffraction peaks align with a tetragonal rutile structure (space group: $P4_2/mnm$)[191], while $LaNiO_3$ exhibits a rhombohedral perovskite structure (space group: R-3c)[192]. The absence of impurity phases and the sharpness of the peaks confirm the phase purity and crystal growth.

Figure 6.2(b) illustrates the XRD pattern of the SLN composites. The diffraction peaks confirm the coexistence of both SnO_2 and $LaNiO_3$ phases in all the composites, with no detectable secondary phases. In the XRD pattern of SLN10, mainly peaks of SnO_2 phase are seen this is due to low concentration of $LaNiO_3$. As the concentration of $LaNiO_3$ increases (for SLN20 and SLN30), peaks of $LaNiO_3$ phase begin to appear. This indicates that $LaNiO_3$ is present in the composites but have not reacted to SnO_2 to form new phase.

Notably, there is no significant shift in the positions of peaks belonging to SnO_2 and $LaNiO_3$ phases in the composites. No shift in the peak position of $LaNiO_3$ and SnO_2 eliminates possibility of incorporation of any ion from one lattice (SnO_2) to another lattice ($LaNiO_3$) or vice versa. $LaNiO_3$ and SnO_2 coexist as separate phases within the composite. However, a noticeable broadening of diffraction peaks is observed with increasing $LaNiO_3$ content. Peak broadening may be due to reduction in the particle size of the matrix SnO_2 and/or reduction in crystallite size.

The incorporation of $LaNiO_3$ into SnO_2 induces lattice strain due difference in their crystal structures, presence of $LaNiO_3$ may hinder the growth of the particles of SnO_2. According to the Scherrer equation, peak width (β) is inversely proportional to crystallite size (D)[138].

$$D = \frac{0.94\lambda}{\beta cos\theta} \qquad (6.2)$$

The thermal expansion coefficients and crystal structures of SnO_2 and $LaNiO_3$ differ, which can lead to the development of micro strain during heat treatment. $LaNiO_3$, with a thermal expansion coefficient of $11.9 \times 10^{-6}\ K^{-1}$[193], expands faster than SnO_2, which has a thermal expansion coefficient of $8.8 \times 10^{-6}\ K^{-1}$[194]. This mismatch in expansion rates creates internal stresses at the interfaces between the two materials, potentially leading to compressive stresses at the grain boundaries upon cooling. A small amount of $LaNiO_3$ in the SnO_2 matrix can suppress the grain growth of SnO_2 due to the differential expansion. The higher expansion of $LaNiO_3$ prevents the movement and coalescence of SnO_2 grains, effectively hindering their growth. Additionally, $LaNiO_3$ can act as a barrier to grain boundary migration in SnO_2, promoting a more uniform distribution of grains and preventing excessive growth.

Furthermore, Peak broadening caused by lattice strain can be correlated to the electrical properties. This lattice strain is likely originating from the interfacial mismatch between SnO_2 and $LaNiO_3$ particularly at heterointerfaces. At low $LaNiO_3$ content (SLN10), this strain appears to induce defect states associated with semiconducting behavior. As the $LaNiO_3$ fraction increases (SLN20 and SLN30), enhanced strain and interface density may facilitate carrier delocalization, potentially contributing to the observed transition toward metallic-like behavior. These structural effects are indicative of strain-driven modification in charge

transport characteristics, which will be further examined through dielectric and conductivity measurements in the following sections.

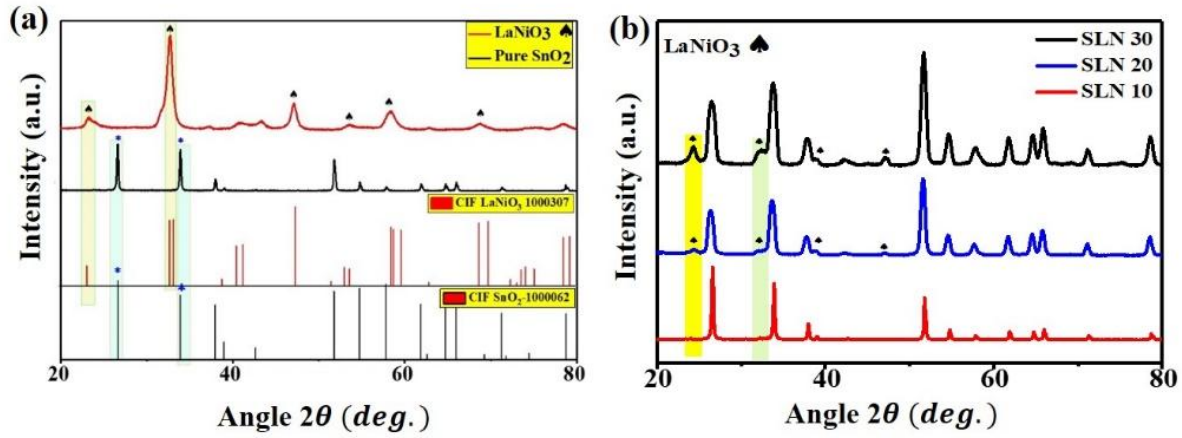

Figure 6.2 X-ray diffraction pattern of (a) individual pure SnO_2 and $LaNiO_3$ compared with the standard CIF files, and (b) SLN composites. As the $LaNiO_3$ content increases, the peak corresponding to $LaNiO_3$ begins to emerge.

6.4 Electrical Properties Measurement

The frequency-dependent relative permittivity of pure SnO_2 and $LaNiO_3$ is presented in Figure 6.3. As observed in Figure 6.3(a), pure SnO_2 exhibits typical insulating behaviour, with the dielectric permittivity (ε') in the range of 10^2 - 10^3. This characteristic response is expected for wide-bandgap semiconductors like SnO_2, where the dielectric constant decreases with increasing frequency due to the limitation of dipolar polarization at higher frequencies.

On the other hand, $LaNiO_3$, as shown in Figure 6.3(b), exhibits a different behavior, characterized by negative permittivity of the order of 10^7. The negative permittivity is indicative of metallic-like conduction and plasmonic effects within the material, making it a potential candidate as an alternative for traditional metals. Furthermore, the fitted data (red

curves in Figure 6.3(b)) exhibit a strong frequency-dependent response, consistent with Drude-like behavior in $LaNiO_3$, supporting the free-electron conduction mechanism. Overall, the different dielectric responses of SnO_2 and $LaNiO_3$ highlight the fundamental difference between insulating and conducting materials, reinforcing the role of $LaNiO_3$ as a highly conductive and tunable component in composite systems.

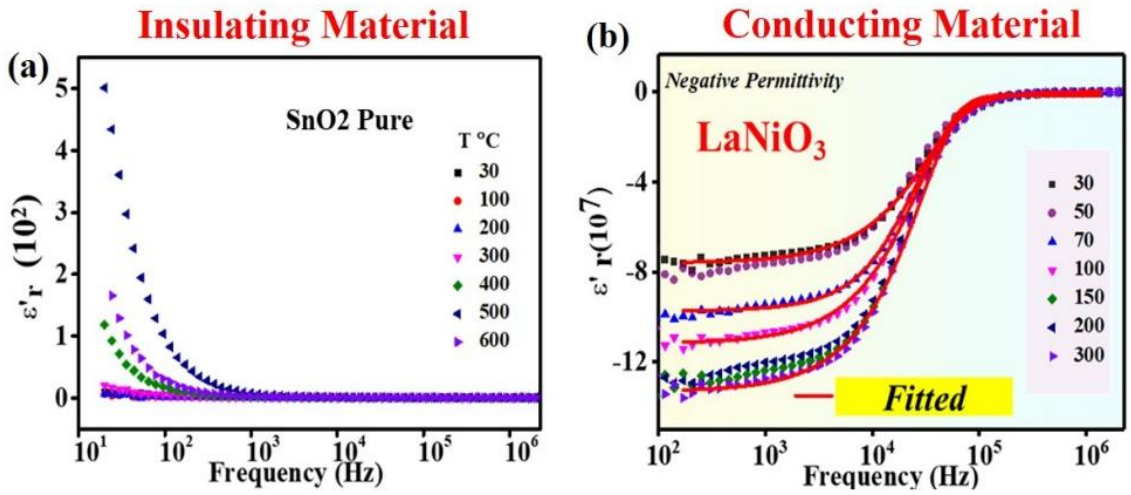

Figure 6.3 Frequency-dependent relative permittivity of (a) pure SnO_2, exhibiting typical insulating behavior with a permittivity range of 10^2 - 10^3, and (b) $LaNiO_3$, demonstrating negative permittivity with a high magnitude (~10^7), indicative of metallic conduction and plasmonic effects. The contrasting dielectric properties highlight the fundamental difference between the two materials.

The electrical properties of SLN composites were measured using an LCR meter over a frequency range of 100 Hz to 2 MHz and a temperature range from room temperature (RT) to 600°C. Impedance was measured, and the effective permittivity of the composites was calculated using standard mathematical relations.

We know that permittivity is related to impedance according to equation (6.3) [195];

$$\varepsilon_r' = -\frac{Z''}{2\Pi f C_o\left[\left(Z'^2\right) + \left(Z''^2\right)\right]} \qquad (6.3)$$

Where, Z' and Z'' are real and imaginary parts of the impedance, C_0 is the vacuum capacitance, and f is test frequency. From the above equation it is clear that the sign of Z'' is same as of ε_r'.

Figure 6.4 illustrates the relative permittivity $\varepsilon_r'$of the composites as a function of frequency (f) at different temperatures (T).

For the SLN10 sample, measurements were performed from RT to 600 °C to examine whether negative permittivity could emerge at higher temperatures due to the thermal excitation of charge carriers, as observed in previous studies[138]. The dielectric response of the composite, shown in the Figure 6.3(a), indicates that the relative permittivity (ε_r')remains positive and exhibits two distinct relaxation processes within the investigated frequency range.

The primary relaxation mechanism observed is attributed to ***space charge polarization***, which is most probable in the measured frequency range[196,197]. In this composite, interfacial polarization can occur at three interfaces: (***i***) the sample-electrode interface, (***ii***) the interface between SnO_2 and $LaNiO_3$, and (***iii***) the grain-grain boundaries of SnO_2. Each of these interfaces is expected to have different relaxation frequencies and times.

Interfacial polarization, or Maxwell-Wagner-Sillars (MWS) polarization, arises at interfaces between electrodes and the sample on a macroscopic scale or between grain and grain boundaries on a microscopic scale. Regions with different electrical conductivities, such as between grains and grain boundaries in polycrystalline materials as SLN 10 here, the conductive $LaNiO_3$ grains and insulating SnO_2 grain boundaries create a conductivity contrast

that causes charge carriers from the $LaNiO_3$ phase to accumulate at the SnO_2 interfaces. This charge trapping leads to significant interfacial polarization, which influences the material's dielectric behavior, especially at low frequencies (< 10^3 Hz). It is reported that in polycrystalline SnO_2 gains are more conductive due to significant number of oxygen vacancies, while the grain boundaries are insulating[197], hence interfacial polarization at grain-grain boundaries result in. The charge accumulation resulting from difference in the conductivity produces interfacial polarization leads to high dielectric constant(ε_r').

Furthermore, we can also see a plateau region in the frequency range of 10^4–10^5 Hz, corresponding to the intrinsic dielectric response of the composite, which is temperature-dependent. At 100 °C, the plateau is narrow (10^2–10^3 Hz), indicating a small difference in the relaxation times of two interfacial polarization processes. At 600 °C, a more prominent plateau is observed, reflecting a greater disparity in the relaxation times. This behavior is driven by electron hopping between Ni^{3+} and Ni^{2+} ions in $LaNiO_3$. Higher temperatures facilitate increased charge carrier activation, enhancing electron hopping and yielding a more defined plateau. In contrast, lower temperatures result in reduced activation and a less distinct plateau. At frequencies above 10^5 Hz, permittivity decreases due to orientational polarization, as thermal motion prevents dipoles from reorienting fast enough to keep up with the oscillating electric field[32].

Variation of relative permittivity with frequency for the composite SLN 20 is shown in Figure 6.4 (b). Measurements were limited to 100 °C based on observations of negative permittivity at and around room temperature. From Figure 6.4 (b) it is observed that relative permittivity is negative at all temperatures and frequencies, magnitude increasing as the temperature increases. The SLN 20 composite exhibits negative permittivity, primarily due to the metallic-

like behavior of the $LaNiO_3$ phase, with free charge carriers contributing to a Drude-like response. At lower frequencies (<10^4 Hz), high negative permittivity values are observed, which decrease gradually at higher frequencies. This decrease is a result of the inability of charge carriers (electrons) in the conductive $LaNiO_3$ phase to follow the rapidly oscillating electric field at higher frequencies, leading to a reduction in the negative permittivity.

In Figure 6.4 (c), negative permittivity behavior was consistently observed in the SLN30 composite from RT to 100°C. The response of relative permittivity to frequency is almost same for both the composites SNL20 and SNL30. This temperature range was selected to investigate the temperature dependence of negative permittivity and to ensure the thermal stability of the composites at higher temperatures.

In 1900, Paul Drude proposed a model to explain the negative permittivity behavior of metals. According to the Drude's model, relative permittivity is given as[121]:

$$\varepsilon_r' = 1 - \frac{\omega_p^2}{\omega_\tau^2 + \omega^2} \qquad (6.4)$$

Where,

$$\omega_p = \sqrt{\frac{n_{eff}.e^2}{m^{*2}.\varepsilon_0}} \qquad (6.5)$$

Where ω_τ is the damping frequency which is related to the relaxation time (τ) by the relation $\omega_\tau = 1/\tau$. It represents the characteristic frequency at which charge carriers lose momentum due to collisions, and ω_p is the Drude plasma frequency that is associated with the density of free carriers (n_{eff}), electronic charge (e), and effective mass (m*).

Researchers have extensively applied The Drude model to fit experimental data observed for complicated composites and single-phase materials[108]. We have also applied this model to explain the experimental results of SLN20 and SLN30. For the fitting, we used **OriginPro 17** and employed the **Levenberg-Marquardt method** to fit the experimental data. In Figure 6.4 (b), and (c) symbols are experimental data and solid lines are data generated according to the Drude model (eqn. 6.4). A good matching between theoretical and experimental data points confirms the validity of the model. The maximum permittivity for SLN20 is $\boldsymbol{\varepsilon_r' = -30 \times 10^2 \pm 4\%}$, while for SLN30 it is $\boldsymbol{\varepsilon_r' = -1.5 \times 10^5 \pm 2.2\%}$. This indicates that the fitting error is less than 5%, suggesting a strong agreement between the experimental data and the theoretical model.

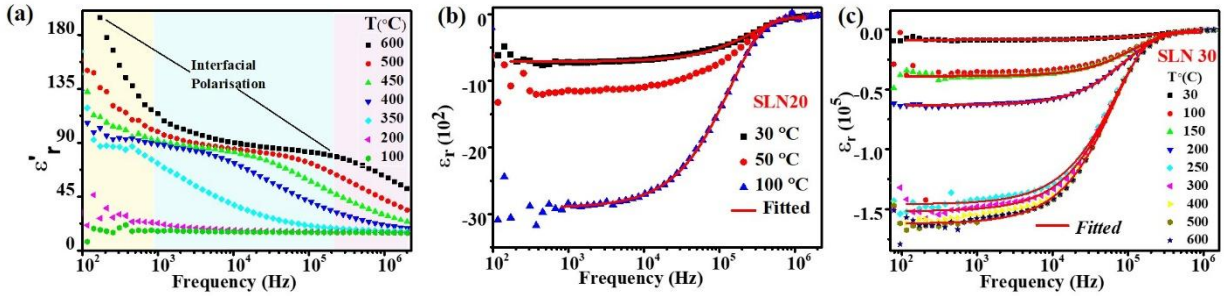

Figure 6.4 Variation of relative permittivity with respect to frequency at various temperatures for (a) SLN10, (b) SLN20, and (c) SLN30. It is confirmed that when the $LaNiO_3$ content exceeds 10%, negative permittivity is observed.

From the fitting, a key parameter that can be derived is the plasma frequency(ω_p). The plasma frequency is directly related to the density of charge carriers (n_{eff}), and it is therefore closely linked to the onset of negative permittivity. As the number of charge carriers increases, the plasma frequency also increases, leading to a stronger negative permittivity. This trend is clearly demonstrated by the fitting results: the plasma frequency for SLN20 is ~ $\boldsymbol{3.7\ GHz}$,

while for SLN30, it increases significantly to $\sim 23\ GHz$. However, another parameter from eqn. (6.4), the damped frequency (ω_τ), decreases as negative permittivity increases. For SLN20, this value is 98 MHz, while for SLN30, it reduces to 6.2 MHz. This trend demonstrates that the material behaves oppositely to metals, supporting its semiconducting nature.

The increase in negative permittivity is directly linked to electrical conductivity. Since EMI shielding is affected by conductivity, material thickness, and frequency, it is essential to investigate how conductivity influences permittivity in our composites. To explore this, we plotted the electrical conductivity as a function of frequency at various temperatures, as shown in Figure 6.5.

Figure 6.5 (a) shows the total conductivity of SLN10 as a function of frequency at various temperatures. The conductivity remains almost constant up to a certain frequency (~10^5 Hz) and then increases sharply at higher frequencies. The constant conductivity at lower frequencies corresponds to the DC conductivity. Frequency dependence of the conductivity can be described by Jonscher's power law, commonly observed in disordered materials.

In Figure 6.5 (b) and (c) variation of conductivity with frequency for composites, SLN 20 and SLN 30 are shown. The conductivity remained constant at lower frequencies (up to 10^5 Hz) but decreased sharply at higher frequencies. This behavior can be attributed to the skin effect, where alternating current (AC) induces eddy currents that oppose the EM wave penetration into the material, leading to current confinement near the surface[198]. This phenomenon is a universal characteristic of metals and as a result, metals typically exhibit a smaller skin depth, restricting the penetration of EM waves and causing a significant portion of the wave to be

reflected due to impedance mismatch at the material boundary. Drude proposed a model to explain the behavior of conductivity in metal:

$$\sigma_{ac} = \sigma_{dc} \frac{\omega_\tau^2}{\omega^2 + \omega_\tau^2} \qquad (6.6)$$

We applied eqn. (6) for conductivity to fit the experimental data, as shown in Figures 6.5(b) and 6.5(c). The strong agreement between the experimental data (symbols) and theoretical predictions (solid lines) suggests that the observed permittivity and conductivity are attributed to the plasma oscillations of free (delocalized) electrons. The plasma frequency extracted from the fitting is approximately $\omega_p \sim 10^9$ Hz, while the damping frequency is around $\omega_t \sim 10^6$ Hz.

Recently synthesized negative permittivity composites, along with their corresponding dielectric constants and AC conductivities, are summarized in Table 6.1.

Table 6.4. Comparative summary of recently developed composites and their corresponding dielectric constants and AC conductivities.

S.N.	Composites	Dielectric Constant	A.C. Conductivity (S/cm)	Frequency range	Ref.
1	In doped-SnO_2	-12 to -1.25	40 to 11	10 MHz- 1GHz	[199]
2	Sb doped SnO_2 (doped ceramics)	-200 to -2.5	10^{-3} to 10^{-1}	200 MHz – 1GHz	[108]
3	Ni/ Al_2O_3	-6 to 0.02	Not Available	200 MHz- 1 GHz	[24]
4	Ni/$BaTiO_3$	+53 to - 153	14 to 300	200 MHz to 1GHz	[25]
5	Ni/ Cu/ Zn	50 - 310	Not Available	3-6 (log frequency)	[200]
6	Graphene/ PVDF	-7250	10^{-6} to 1	200 MHz to 1 GHz	[201]
7	Graphene/ PDMS	-61250 to -40855	10^{-6} to 10^{-3}	10 kHz-1MHz	[202]
8	MWCNTs/ PDMS	300 to – 40	10^{-2} to 100	10 MHz- 1 GHz	[203]
9	MWCNTs/ TiN/ CCTO	-200	1000 to 100	90 MHz- 683 MHz	[204]

10	Ag/Al_2O_3/ 3D $BaTiO_3$/ Epoxy	-4 to 0	2 x10^{-2} to 10	10 kHz – 1 MHz	[205]
11	Ti_3AlC_2/ Polyimide	-1200 to 0	0.1 to 100	10 MHz – 1 GHz	[206]
12	SnO_2/ $LaNiO_3$	+1000 to -1.5 x 10^5	1.8 x 10^{-3} to 4500	100 Hz to 2 MHz	**This work**

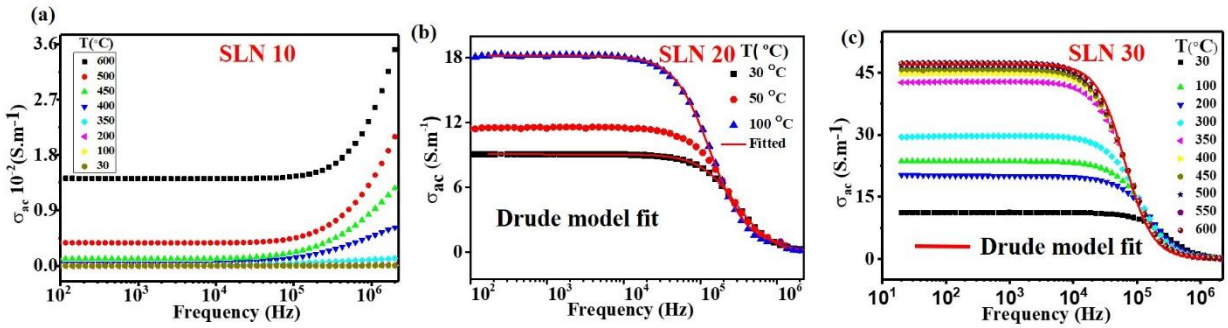

Figure 6.5 Variation of relative permittivity with respect to frequency at various temperatures for (a) SLN10, analogs to Jonscher's power law, (b) SLN20, and (c) SLN30 showing skin effect when filler content exceeds 10%.

6.5 X-ray Photoelectron Spectroscopy (XPS) Analysis

To investigate the chemical states of the elements, present in the composite, XPS measurements were conducted, and the corresponding spectra are presented in Figure. 6.6. A crucial observation from the data is that there is no significant shift in the binding energies or their positions. This confirms the absence of any strong chemical interactions between SnO_2 and $LaNiO_3$, indicating that the composite formation primarily involves physical mixing rather than chemical bonding.

Figure 6.6(a) displays the Ni 2p XPS spectra, where characteristic peaks corresponding to Ni^{3+} $2p_{3/2}$ and Ni^{2+} $2p_{3/2}$ are observed. Additionally, satellite peaks (sat.) associated with these oxidation states appear around 872 eV for the Ni^{3+}/ Ni^{2+} $2p_{1/2}$ states[147]. The presence of both oxidation states indicates a mixed-valence nature of Ni in the composite, which is consistent with the expected electronic structure of $LaNiO_3$. Notably, a similar spectral profile is observed for SLN30, with no major differences in peak positions or intensities, reinforcing the conclusion that the $LaNiO_3$ phase remains chemically unaltered in the SnO_2 matrix.

Figure 6.7(b) illustrates the Sn 3d core-level spectra, where two distinct peaks at approximately 486.6 eV and 495 eV correspond to Sn^{4+} $3d_{5/2}$ and Sn^{4+} $3d_{3/2}$, respectively[207]. The sharp and symmetric nature of these peaks confirms the dominance of the Sn^{4+} oxidation state, indicating that the SnO_2 phase remains consistent. The binding energy values align well with previously reported values for SnO_2, further confirming the stability of the tin oxide phase in the composite[207].

Overall, the XPS analysis reveals that no noticeable chemical reaction occurs between SnO_2 and $LaNiO_3$, and both phases retain their inherent oxidation states in the composite system.

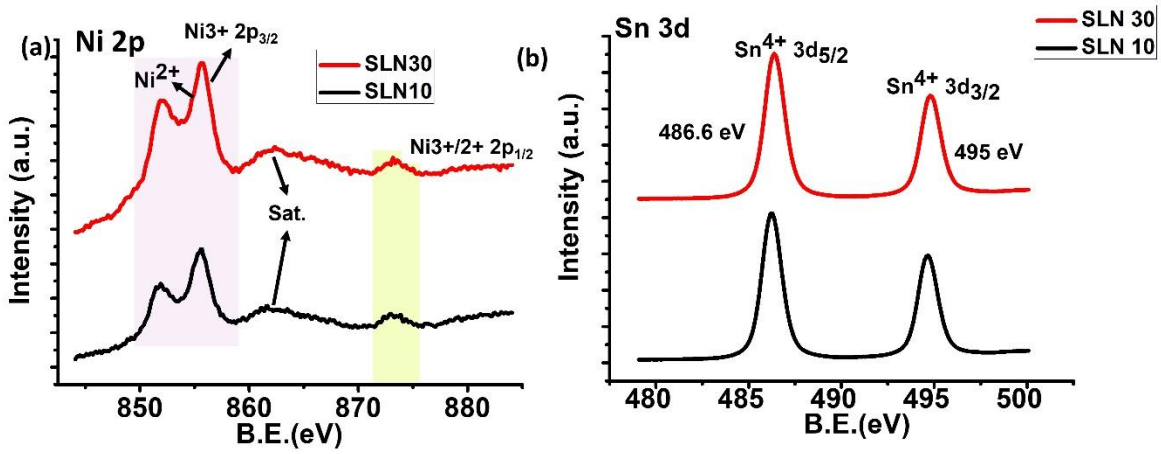

Figure 6.6 XPS spectra of the prepared composites. (a) Ni 2p spectrum showing Ni^{3+} and Ni^{2+} oxidation states along with their satellite peaks, confirming the mixed-valence nature of Ni in the composites. (b) Sn 3d spectrum displaying Sn^{4+} peaks, indicating the chemical stability of SnO_2 in the composite without significant interaction with $LaNiO_3$.

6.6 D.C. Conductivity Analysis

After conducting the electrical conductivity measurements of the SLN composites, we further analysed the DC conductivity (σ_{DC}) by plotting it against the inverse temperature ($1000/T$) to extract the activation energy (E_a) using the Arrhenius equation[208]:

$$\sigma_{DC} = \sigma_0 \exp(-\frac{E_a}{k_\beta . T}) \qquad (6.7)$$

Where E_a is the activation energy, σ_0 is a constant, k_B is Boltzmann constant and T is temperature. To extract E_a, the eqn. 6.7 was linearized as $\boldsymbol{log\,\sigma_{DC} = log\,\sigma_0 + E_a/K_B.T}$. The slope of the linear plot of $\log(\sigma_{DC})$versus $1000/T$ provided the activation energy.

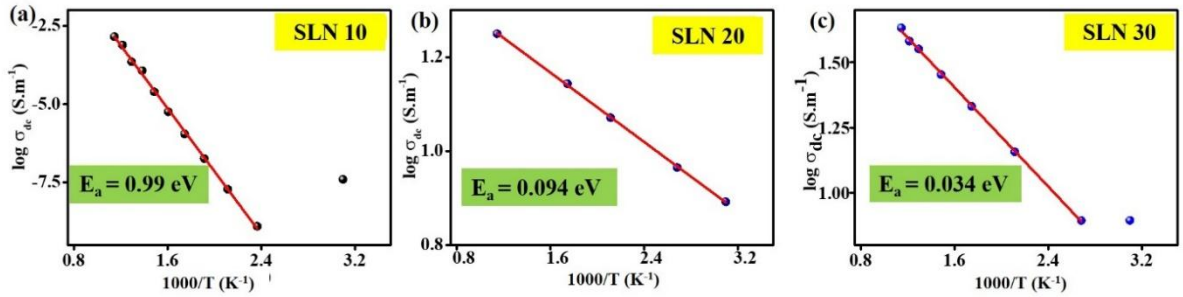

Figure 6.7 Variation of DC conductivity of the composites with the inverse of temperature for (a) SLN10, (b) SLN20, and (c) SLN30. The solid lines represent linear fits. A systematic decrease in activation energy is observed as the conductivity.

The activation energy of the synthesised composites has shown in Figure 6.7. In the SLN10 composite, the activation energy of approximately 0.99 eV suggests that charge transport is primarily governed by doubly ionized oxygen vacancies characteristic of insulating SnO_2. As the $LaNiO_3$ content increases, the activation energy decreases, reaching 0.094 eV in SLN20 and 0.034 eV in SLN30. For single-phase $LaNiO_3$ activation, energy is found to be 0.019 eV and conduction mechanism is hopping of small polaron[36]. Same order of the activation energy for the composites SNL20 and SNL30 indicates that $LaNiO_3$ dominates conduction in these composites although its concentration is low. X-ray photoelectron spectroscopy (XPS) analysis reveals the presence of nickel in both Ni^{3+} and Ni^{2+} oxidation states, which is characteristic of the multi-valent nature of $LaNiO_3$. The low activation energy in SLN30 shows a nearly continuous conductive network, which improves charge carrier transport. As a result, SLN30 exhibits higher conductivity than SLN10 and SLN20 due to better electronic connectivity.

Increasing the $LaNiO_3$ concentration reduces the activation energy, indicating the formation of additional percolative/conductive pathways, as confirmed by SEM analysis of the composites.

6.7 Microstructure and Percolation Pathways

The SEM micrographs of pure $LaNiO_3$, SnO_2, and their composites (SLN10, SLN20, and SLN30) shown in Figure 6.8. In Figure 6.8, (a) pure $LaNiO_3$ has a dense microstructure with 97% experimental density and about 3% porosity. This compact structure supports efficient charge transport. The average particle size is calculated **via ImgJ** software is in the range 90-130 nm. In contrast, pure SnO_2**,** displays a granular morphology typical of its insulating nature shown in Figure 6.8 (b). The average particle size distribution of is shown in the inset of Figure 9 (a) and (b). As a wide-band gap semiconductor, SnO_2 does not have free charge carriers for electronic conduction. In Figure 6.8 (c), SLN10, the microstructure shows a sparse distribution of conducting nano sized $LaNiO_3$ particles in the SnO_2 matrix. At this concentration, conducting $LaNiO_3$ grains are isolated, and no continuous network is formed[56]. The charge carriers cannot move freely over long distances, preventing the negative permittivity response. Figure 6.8 (d)**,** reveals that in SLN20**,** the $LaNiO_3$ nano sized particles are more closely distributed, allowing charge carriers to move between neighbouring particle through tunnelling [27,209]. This behaviour is due to the mixed valence states of Ni, which support electron movement between Ni^{2+} and Ni^{3+}. A significant difference the micrograph of SLN30 can be observed in Figure 6.8 (e)**,** where the $LaNiO_3$ grains form continuous pathways. This network allows charge carriers to move with much lower resistance in the SnO_2 matrix, shifting the transport from hopping to metallic conduction. The presence of these conductive paths leads to an increase in negative permittivity and conductivity.

Bulk densities of the composites were measured using **Archimedes' principle**. Each sample was weighed in air and while fully submerged in deionized water measurements were repeated three times and the mean value reported. The experimental densities of SLN composites are; SLN10~ 6.66±.07, SLN20~ 6.75± 0.11, SLN30~ 6.82± 0.06 respectively.

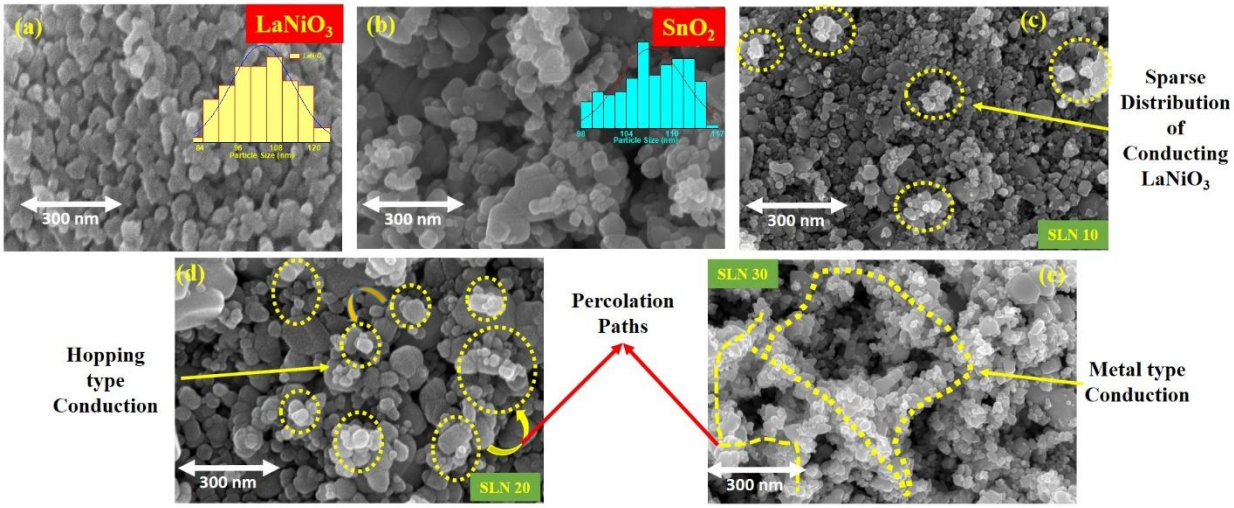

Figure 6.8. Microstructure of freshly fractured samples: (a) pure $LaNiO_3$, exhibiting dense and well-defined grains; (b) pure SnO_2; (c) SLN10, showing isolated $LaNiO_3$ particles within the SnO_2 matrix; (d) SLN20, revealing the formation of conductive pathways between phases; and (e) SLN30, demonstrating metallic-like continuous conduction due to the increased concentration of nanosized $LaNiO_3$ particles.

6.8 EMI Shielding Effectiveness Study

The EM shielding primarily involves the reflection and absorption of EM waves interacting with materials. The shielding effectiveness of the material is calculated using S-parameters (S_{11}, and S_{21}), that provide direct insight into how well a material reflects and transmits electromagnetic waves, which are essential factors in determining its shielding performance, making S-parameters a widely adopted method for reliable and reproducible EMI shielding

analysis. The reflection coefficient (S_{11}) measures the portion of the incident electromagnetic wave that is reflected back from the material's surface, while the transmission coefficient (S_{21}) indicates the amount of wave that passes through the material.

In the context of EMI shielding, a higher reflection coefficient (S_{11}) means the material is more effective at reflecting electromagnetic waves, preventing them from penetrating the material. Conversely, a lower transmission coefficient (S_{21}) indicates better blocking of electromagnetic waves from passing through, which is a key requirement for effective shielding.

Total shielding effectiveness (SE_T) would be given by[210–212]:

$$SET = SEA + SER \qquad (6.8)$$

we calculated SE_R (reflection loss) and SE_A (absorption loss), using the relations:

$R = |S_{11}|^2$, $T = |S_{21}|^2$, $A = 1 - R - T$, $SE = -10\log_{10}(T)$, $SEr = -10\log_{10}(1 - R)$,

$$SE_A = 10\log\left(\frac{10^{\frac{S21}{10}}}{1 - 10^{\frac{S11}{10}}}\right) \qquad (6.9)$$

$$SE_R = 10\log\left(1 - 10^{\frac{S11}{10}}\right) \qquad (6.10)$$

Where SE_A is shielding due to absorption, and SE_R shielding due to reflection.

The shielding effectiveness of the prepared composites shown in Figure 6.9. Pure epoxy demonstrates minimal interaction with incoming EM waves, with both reflection and absorption values below 5 dB. This indicates that pure epoxy allows most of the EM waves to pass through with little attenuation, resulting in limited shielding effectiveness.

Figure 6.9 (a) shows the shielding effectiveness of the composites in absorption mode (SE_A), where SLN10 and SLN20 exhibit significant effectiveness due to their enhanced ability to absorb electromagnetic waves. Nano-sized $LaNiO_3$ particles dispersed within a SnO_2 matrix. The $LaNiO_3$ nanoparticles, due to their high conductivity and negative permittivity, act as tiny reflective surfaces for the incident EM waves. As these waves interact with the $LaNiO_3$ particles, multiple reflections occur between the nanoparticles. This repeated reflection facilitates energy dissipation, mostly through absorption, thereby increasing the overall shielding effectiveness. The maximum SE of SLN 10 and 20 is around 40 dB. Figure 6.9 (b) presents the shielding effectiveness in reflection mode (SE_R), where composites with higher negative permittivity i.e. SLN 30 demonstrate better reflection. This is due to their conductive nature and impedance mismatch at the material interface, which enhances the reflection of electromagnetic waves. As a result, SLN30 primarily reflects EM waves, achieving a maximum shielding efficiency of approximately 35 dB. A graphical interpretation of the shielding mechanisms through absorption, and reflection shown in Figure 6.9 (c) and 6.9 (d), respectively.

To further understand the shielding behavior of the composites, we consider the role of skin depth ($\boldsymbol{\delta = \sqrt{(2 / (\mu \sigma \omega))}}$), which is defined as the distance over which the amplitude of an electromagnetic wave decays to $1/e$ of its surface value[171,198]. Although direct calculation of δ is limited by the lack of permeability measurements, its qualitative dependence on conductivity provides useful insight. The skin depth is inversely proportional to the conductivity, and thus decreases with increasing electrical conductivity. As a result, highly conductive materials like metals, restrict field penetration to a shallow surface region, enhancing reflection-based shielding. In the present study, SLN30 shows the highest

conductivity among the samples, consistent with its lower skin depth and stronger reflective behavior. Conversely, SLN10, with lower conductivity and larger skin depth, exhibits dominant absorption characteristics. This correlation between conductivity, skin depth, and shielding mechanism highlights the transition from absorption-dominated to reflection-dominated behaviour across the composite series. Moreover, in the presence of negative permittivity, the suppression of wave propagation is further reinforced by the formation of evanescent modes, which decay exponentially within the material.

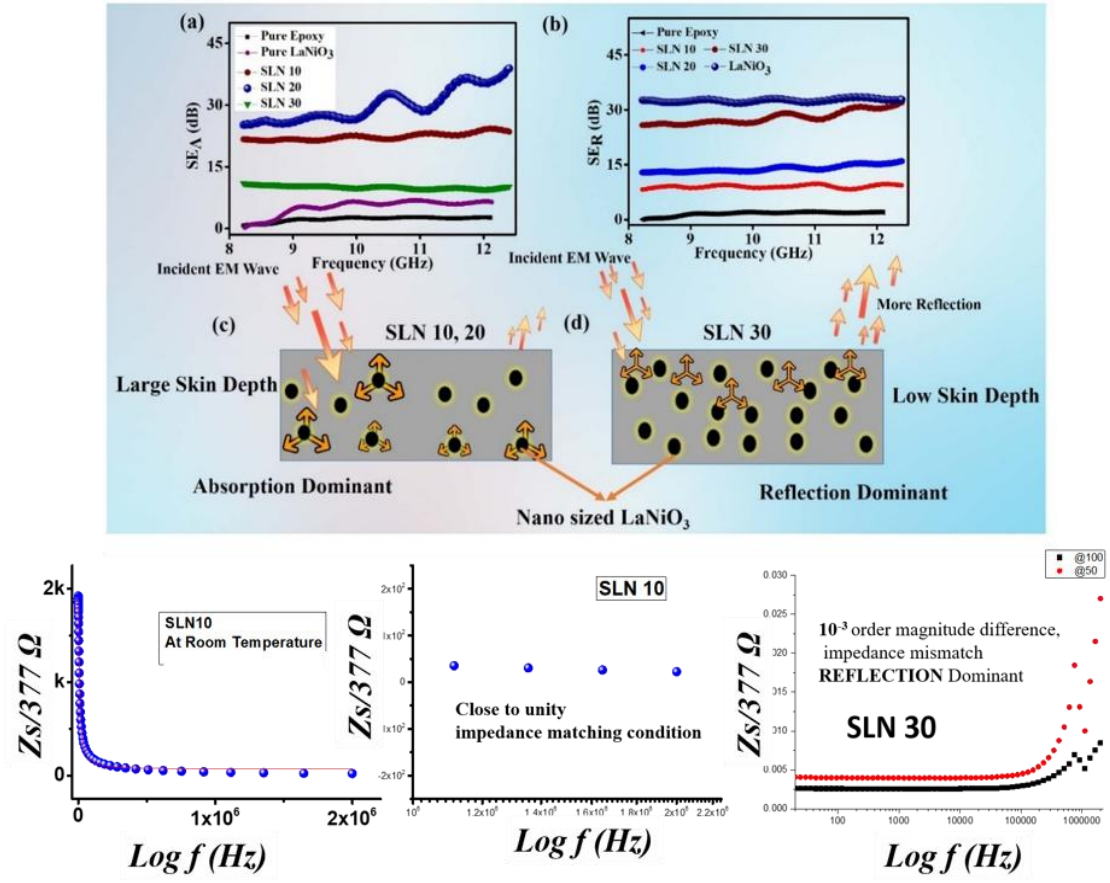

Figure 6.9 Shielding effectiveness of the composites: (a) in absorption mode and (b) in reflection mode. A lower concentration of filler enhances absorption, while higher conductivity in SLN30 improves reflection of electromagnetic waves, similar to the effect of a Faraday cage. The shielding behavior can also be verified by normalized impedance analsysis for SLN10 and SLN30.

Note: [Volume Fractions, Percolation, and Reproducibility]

To enhance reproducibility, we are providinge a detailed information of volume fractions, calculated from measured densities (SnO_2 = 6.95 g/cm³, $LaNiO_3$ = 7.01 g/cm³, epoxy = 1.15 g/cm³). For example, SLN10 contains ~3.95 vol% $LaNiO_3$, ~35.86 vol% SnO_2, and ~60.19 vol% epoxy.

- **Percolation:** DC conductivity measurements indicate a sharp percolation threshold at **≈ 4–5 vol%** $LaNiO_3$. While ceramic composites typically exhibit higher thresholds, our dense, highly conductive $LaNiO_3$ grains form connected paths at unusually low volume fractions. This early onset of percolation provides the structural basis for the transition in shielding mechanism.
    - **SLN10 (~4 vol% $LaNiO_3$):** Near φ_c, the weakly percolated network in an insulating matrix produces a lossy dielectric environment favorable for absorption.
    - **SLN30 (~12 vol% $LaNiO_3$):** Far above φ_c, the continuous conducting network supports negative permittivity and plasmonic-like behavior, resulting in dominant reflection.
- **Binder properties:** The pure epoxy matrix was measured to have a bulk resistivity of **$\rho \approx 4.8 \times 10^{12}$ Ω·m**, consistent with literature values (10^{11}–10^{14} Ω·m). The sample thickness was kept constant at **t = 2.00 mm**, ensuring comparability across measurements.

To gain a deeper understanding of the physics and mechanisms behind the EMI shielding mechanism, it is essential to examine the impedance characteristics of the composite materials.

6.9 Impedance Characteristics

When an electromagnetic (EM) wave propagates from one medium (e.g. air) to another with lower impedance, impedance mismatch occurs, causing partial reflection and transmission at the interface due to differences in permittivity and permeability. In conducting materials, the skin effect limits the penetration of the electric field, preventing deep penetration of the wave. Metals, having lower impedance than air, reflect the wave at the boundary, resulting in a phase shift of 180° (π radians) relative to the incident wave.

Impedance of a material is given by[14,213]:

$$Z_{material} = \sqrt{\frac{\mu_0.\mu_r}{\varepsilon_0.\varepsilon_r}} \qquad (6.11)$$

Where μ_0, ε_0 are the permeability and permittivity of free space, and μ_r, ε_r (ε_r =ε/εo) are the relative permeability and permittivity of the medium, respectively.

For ε < 0:

$$z_{ENG} = \boldsymbol{i} z_0 \sqrt{\frac{\mu_r}{|\varepsilon_r|}} \qquad (6.12)$$

$Z_{material}$ becomes imaginary, referred as impedance mismatch. Where $z_0 = \sqrt{\frac{\mu_0}{\varepsilon_0}}$ is the impedance of free space (~377 ohm).

To investigate how impedance influences wave behaviour, we conducted impedance measurements using an LCR meter to analyse the frequency-dependent impedance characteristics of the prepared composites. The measurements focused on two parameters, including the phase angle (ϕ) and the real and imaginary components of impedance (Z'/Z''). We selected two composites for comparison: SLN10, a conventional dielectric with positive permittivity, and SLN30, with negative permittivity.

In Figure 6.10 (a) Nyquist plot for SLN 10 at three temperatures 400 °C, 500 °C, and 600 °C shown. Due to the high resistance of SLN10, were unable to record this plot at low temperatures (< 400 °C). At all temperatures, a semi-circular arc (centre below Z′) is observed. However, diameter of the semicircle decreases with increasing temperature. Decrease in semicircle diameter is due to decrease in the resistance because diameter is representation of resistance. In contrast to SLN10, the Nyquist plot (in the Z" vs. Z' plot) for SLN30 exhibits a constant upward trend with increasing frequency, forming a straight line rather than the typical semi-circular arc as shown in Figure 6.10 (b). Upward trend is an indication of inductive nature of the composite SLN30. We know that inductive reactant of an inductor $X_L = \omega L$, increases with increasing frequency[104].

Variation of imaginary impedance (Z") with frequency for SLN10 and SLN30 are shown in Figure 6.10 (c) and (d). For SLN10, a pronounced peak is observed whose position shifts towards high frequency side with increasing temperature. This is a typical feature of a thermally activated relaxation process. Thermally activated free charge carriers reduce the energy storage contribution by shortening the relaxation time ($\tau = RC$) in materials where resistance decreases with temperature, such as semiconductors. As the temperature increases, charge carriers enhance conductivity, lowering the resistance (R). This reduction in resistance leads to a

decrease in relaxation time (τ), and consequently, the frequency of oscillations or responses in an RC circuit increases, since τ = RC and a decrease in R results in a shorter τ. However, it's important to note that for metals, the resistance generally increases with temperature, which would lead to an increase in relaxation time. In contrast, SLN30 exhibits a monotonically increasing (Z") trend with frequency due to inductive nature. The absence of a relaxation peak suggests that inductive effects dominate over polarization mechanisms. Additionally, the temperature dependence of (Z") in SLN30 is minimal, highlighting the stability of its inductive response compared to the thermally sensitive capacitive behaviour of SLN10. This distinct behaviour emphasise the tunability of electrical properties of SLN composites.

The phase angle (ϕ) is the angle between applied voltage and the resulting current, revealing the contributions of reactive and resistive components to the impedance. Figure 6.10(e), a positive phase angle in SLN10 indicates dominance of ***capacitive reactant***. In contrast, phase angle for SLN30 at all frequencies is negative, a characteristic of ***inductance*** Shown in Figure 6.10 (f). As temperature increases, the phase angle for SLN10 increases across frequencies due to increase in conductivity because of thermally excited charge carriers. These results highlight the distinct dielectric behaviours of SLN10 and SLN30, with phase angle analysis.

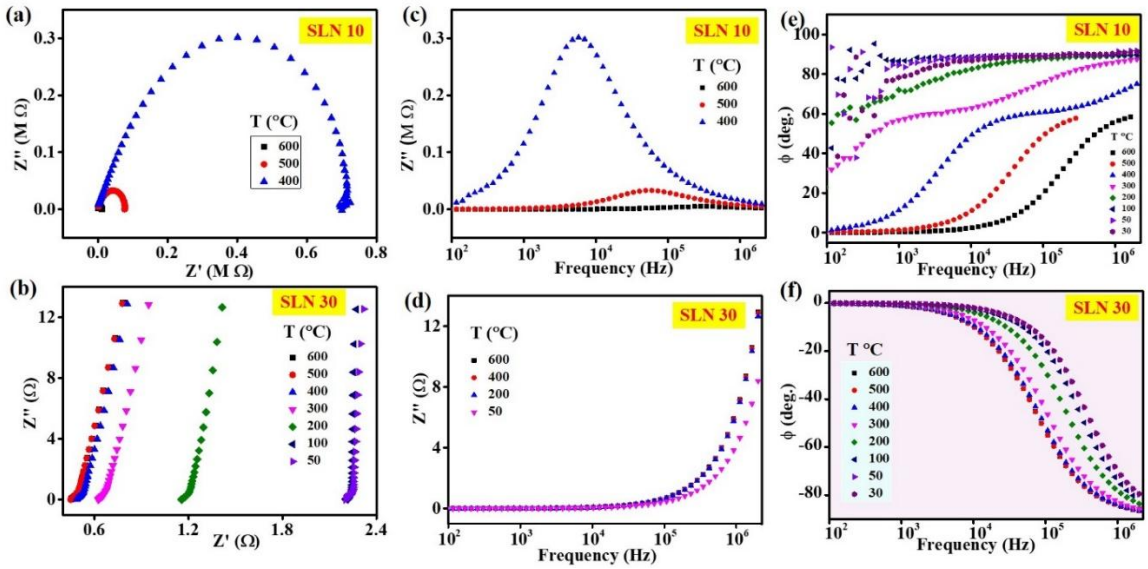

Figure 6.10 Schematic comparison of impedance characteristics for SLN10 and SLN30. (a) and (b) show the variation of imaginary impedance (Z") with real impedance (Z') for SLN10 and SLN30, respectively. (c) and (d) depict the variation of Z" with frequency. (e) and (f) illustrate the phase angle variation. The negative phase angle in SLN30 indicates a shift between positive and negative permittivity.

6.10. Conclusion

In conclusion, SnO_2:$LaNiO_3$ (SLN) composites present a promising alternative to traditional metal and carbon-based EMI shielding materials. By replacing conventional fillers with $LaNiO_3$, we have tuned permittivity of SnO_2 from positive to negative. This result is facilitated by the formation of conductive networks/percolating paths within the insulating SnO_2 matrix. SEM analysis revealed that increasing $LaNiO_3$ creates conductive percolating paths, significantly improving conductivity. Negative permittivity is achieved with as low as 20% $LaNiO_3$ content, owing to the nanoscale size of $LaNiO_3$ and SnO_2, which provides a large surface-to-volume ratio. SLN10 exhibited positive permittivity and having shielding effectiveness of approximately 40 dB in absorption mode, attributed to better impedance matching. In contrast, composite SLN30 (with 30% $LaNiO_3$) demonstrates shielding

effectiveness (30 dB) in reflection mode due to impedance mismatching. The ability to tune the shielding mechanism—whether absorption or reflection—by adjusting filler content offers a flexible platform for designing EMI shielding materials for various applications. Future work will explore tuning filler content and ceramic composition through doping or synthesis optimization to enhance EMI performance, with potential to realize epsilon-near-zero materials for near-perfect absorption. These findings highlight the potential of conducting ceramic composites as a new class of materials with multifunctional properties, overcoming the limitations of traditional composites while providing enhanced performance for low-dimensional and high frequency applications.